Additive Manufacturing Letters 11 (2024) 100244

Contents lists available at ScienceDirect

Additive Manufacturing Letters

journal homepage: www.elsevier.com/locate/addlet

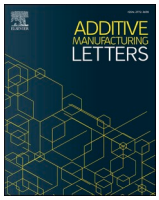

Short Communication

Effect of laser parameters and shielding gas flow on co-axial photodiode-based melt pool monitoring signals in laser powder bed fusion

Joni Reijonen

VTT Technical Research Centre of Finland Ltd., Advanced Manufacturing Technologies, Espoo, FI-02044, Finland
University of Turku, Department of Mechanical Engineering, Turku, FI-20014, Finland

ARTICLE INFO

Keywords:
Laser powder bed fusion
Co-axial
Melt pool monitoring
Photodiode
Vapor plume

ABSTRACT

Melt pool monitoring using co-axial photodiodes is increasingly used for online quality monitoring in PBF-LB AM. However, the fundamental correlations between different processing conditions and the co-axial photodiode signals are not well understood. In this study the impact of laser parameters and the shielding gas flow speed on co-axial photodiode-based melt pool monitoring signals is established. It is shown that laser power has positive linear correlation with the photodiode signal, while the correlation with scanning speed is non-linear in the form of $y=ax^{-b}$. The focal point position, scanning orientation and shielding gas flow speed have highly non-linear response on the photodiode signal, depending on the combinatorial effects of the parameters. These underlying physical correlations should be carefully assessed and taken into consideration when trying to establish correlations between photodiode-based melt pool monitoring signal and defect formation in the PBF-LB process.

1. Introduction

Laser powder bed fusion (PBF-LB) additive manufacturing (AM) is increasingly used as a manufacturing process for making end-use components in industries such as aerospace, where quality requirements are stringent. Although static tensile properties that match, or even surpass those of conventionally manufactured counterparts have been reached for certain alloys processed with PBF-LB [1,2], the high variation in the properties (i.e. low quality) between parts remains a challenge. This is especially the case for dynamically loaded components, where fatigue life is of utmost importance. Berez et al. [3] reported extremely high variation in fatigue life of 17–4 PH stainless steel specimens manufactured at different locations of the building platform, while using a commercial PBF-LB machine and constant parameters optimized by the respective machine manufacturer for the given alloy. The variability in fatigue life between specimens was attributed to the respective variability in porosity between the specimens. Especially lack-of-fusion defects close to specimen surface were identified as detrimental to fatigue life. Process by-products in the form of spatters and condensate from the vapor plume, and specifically differences in how efficiently they are removed by the shielding gas flow, were identified as the likely cause for increased defect density at certain locations. Same observation was made by Moran et al. [4] for Ti-6Al-4 V, where the spatial inhomogeneity in defect densities at different locations of the build plate was also attributed to inhomogeneity in the shielding gas flow. Insufficient shielding gas flow in PBF-LB has been shown to result in dramatic loss of penetration, leading to increased lack of fusion porosity [5].

Due to the generation of such stochastic defects in the PBF-LB manufactured specimens and their detrimental effect on properties such as fatigue life, process monitoring has been extensively pursued as a means to identify local disturbances in the process, which could indicate defect formation [6]. In a recent study by Snow et al. [7] it was shown that process monitoring based on NIR-sensitive optical tomography and photodiodes was able to capture local signal anomalies that corresponded with spatters and further, with spatter-induced lack of fusion defects in the final parts verified by x-ray computed tomography. Although the causal relation between signal anomaly and defect was identified and proven statistically significant especially for large defects >300 μm, a considerable number of false positives remained in the monitoring signal. As identified by the authors, further studies would be needed to distinguish such false positives from the data and improve the reliability of the process monitoring for defect detection as a quality assurance method. Therefore, in addition to studies aiming at establishing correlation between signal and defect, it is also necessary to perform in depth studies on how the different processing conditions affect the process monitoring signal, to understand the effect of a certain process phenomenon on the monitored signal response. This could help us discern normal process variations that do not lead to defects, from

E-mail address: joni.reijonen@vtt.fi.

https://doi.org/10.1016/j.addlet.2024.100244
Received 20 August 2024; Received in revised form 12 September 2024; Accepted 19 September 2024
Available online 19 September 2024

such abnormal events that do, and hence reduce the amount of false-positive indications in the monitoring signals.

Here the focus is on specific type of process monitoring for PBF-LB AM, namely melt pool monitoring using co-axial photodiodes. Pioneering research on the method was done at KU Leuven some 10–15 years ago [8,9]. Mercelis [8] showed linear correlation between melt pool surface area and photodiode signal output intensity. Recently, Reijonen et al. established correlations between beam-area normalized melt pool monitoring signal and melt pool width and penetration while varying the input laser energy conditions [10]. As photodiodes are sensitive to the area and intensity (i.e. temperature) of the emitting source (within the spectral range of the sensor), the other important contributor to the output signal is melt pool temperature, as described by Planck's law. The third significant process related factor on the signal output would then be any obstacles (such as spatters and the vapor plume) that are between the melt pool and the optical path to the photodiode, as discussed by Gutknecht et al. [11,12].

Stutzman et al. [13] recently studied the impact of shielding gas flow speed on optical emissions as observed by an off-axis mounted photodiode filtered with a narrowband filter at 520 ± 10 nm in order to specifically observe line emissions that would correspond to atomically excited Cr I peak. In their study, a decrease in shielding gas flow speed led to an increase in the 520 ± 10 nm line spectral emission for nearly all studied power speed combinations. The authors believed this to be due to a presence of a larger plume above the melt pool when shielding gas flow speed was decreased. In other words, they argued that the vapor plume contributes to the optical emissions at 520 ± 10 nm. The role of thermal emissions from the melt pool were discussed and considered inconsequential. This may hold in their case of a narrow spectrum of 520 ± 10 nm, however a wide range of wavelengths from visible to the infrared (450–1800 nm [12–20]) have been used in photodiode-based monitoring of PBF-LB. Furthermore, in their study they were unable to explain the response of the photodiode signal response when scanning speed was varied. Therefore, it would be necessary to establish what is the impact of the vapor plume to the monitored signal on a wider spectrum, and to study in-depth the relationship between the laser scanning parameters and the photodiode signals. This would elucidate our understanding of the fundamental correlations between the laser melting conditions and the photodiode signals, and eventually enable identification of such process emissions that correlate with un-wanted events that lead to defect formation.

2. Materials and methods

Experiments to collect melt pool monitoring data were performed on a SLM 125 HL PBF-LB system from SLM Solutions GmbH retrofitted with PrintRite3D MPM system from Sigma Labs Inc. The MPM system consists of three photodiodes named as TEP low, TEP high and TED. The process emissions are guided to the photodiodes via the Scanlab camera adapter port located right after the galvanometer scanner (Scanlab Intelliscan 25). The SLM 125 HL system uses a dynamic focusing unit (Scanlab VarioScan 40) instead of an F-theta lens to maintain correct focal distance throughout the build area. Therefore, the optical components that deliver the spectral emissions from the process to the photodiodes are the scanner, the camera adapter and a beam splitter (Thorlabs BPD254S-G) which divides the emissions to the sensors. All three photodiodes then have different filters in front of each one to collect only specific wavelength ranges. TEP low has a 636±5 nm bandpass filter, TEP high 650±5 nm bandpass filter and TED has a shortpass filter with a cut-off wavelength at 800 nm in front of the sensor. Finally, the emissions are focused with $f = 25$ mm Plano-Convex lenses (Thorlabs LA1951-A - N-BK7) to the photodiode sensor. All three photodiodes are the same Thorlabs model APD440A with a nominal spectral responsivity between 400 and 1000 nm. For the actual measured spectrum received by each photodiode in this setup the reader is referred to [10]. The photodiode signals were then collected at a sampling rate of 100 kHz along with the scanner xy-position and laser ON/OFF signals and stored layer-by-layer to Hierarchical Data Format version 5 (HDF5) files to allow for mapping the MPM signal to specific lasering locations on the build area.

Table 1 lists the constant PBF-LB processing conditions used in the experiment, along with the variables (laser power, scanning speed, focus position, scanning orientation and shielding gas flow speed) and their value levels for the $3^5 = 243$ specimens in the full-factorial design of experiments. Fig. 1. shows the layout of the specimens on the building platform. The specimens were purposefully located such that they would avoid the center of the build area and populate an area on the build plate where the variation in the distance the specimens have from the origin is minimal, to avoid significant variation that a changing beam tilt angle may have on the spectral emissions that was demonstrated in [21]. The build job consists of 81 rectangular specimens with dimensions of 5 × 5 × 0.9 mm. As the shielding gas flow speed is a global process parameter (affecting all the specimens on the build simultaneously), the speed is altered on three levels along the build height with 10 layer (0.3 mm) intervals, to generate essentially 3 × 81=243 process conditions in one single build job. The specimens were built directly on top of the building platform, without additional support structures.

Mean values from the photodiode signal data were used in the plots of this study. Table A1 (see Appendix A) provides the number of samples, the calculated mean, associated standard deviations and 99% confidence intervals of the data for each specimen. The 99% confidence interval of the mean ($CI_{99\%}$) is calculated as shown in Eq. (1), where x = mean, Z = confidence level, s = standard deviation, n = sample size. The standard deviation is then calculated as shown in Eq. (2), where X = each value.

$$CI_{99\%} = x \pm Z\frac{s}{\sqrt{n}} \tag{1}$$

$$s = \sqrt{\frac{\sum (X-x)^2}{n-1}} \tag{2}$$

The sample size N between the specimens varies due to changes in the scanning speed, as the data acquisition frequency and specimen size,

Table 1
PBF-LB processing parameters during the experiment.

Process parameter	Value(s)	Factor	Number of levels
Powder	316 L, Carpenter Additive, D_{10}=20 μm, D_{50}=31 μm, D_{90}=47 μm	N/A (constant)	N/A (constant)
Re-coater type	Polymer-composite blade (soft, round profile)	N/A (constant)	N/A (constant)
Re-coating speed	216.67 mm/s	N/A (constant)	N/A (constant)
Shielding gas type	Argon 5.0	N/A (constant)	N/A (constant)
Building platform type	316 L, thickness t = 20.4 mm	N/A (constant)	N/A (constant)
Building platform pre-heat temp.	100 °C	N/A (constant)	N/A (constant)
Laser wavelength	1070 nm	N/A (constant)	N/A (constant)
Beam waist diameter	80±6 μm	N/A (constant)	N/A (constant)
Hatch distance	120 μm	N/A (constant)	N/A (constant)
Layer thickness	30 μm	N/A (constant)	N/A (constant)
Laser power	100, 200, 400 W	1	3
Scanning speed	400, 800, 1200 mm/s	2	3
Focal point position	0, –4, –8 mm	3	3
Scanning angle	0, 45, 90° in relation to the y-axis in Fig. 1.	4	3
Shielding gas flow speed	7.0, 3.5, 1.7 m/s	5	3

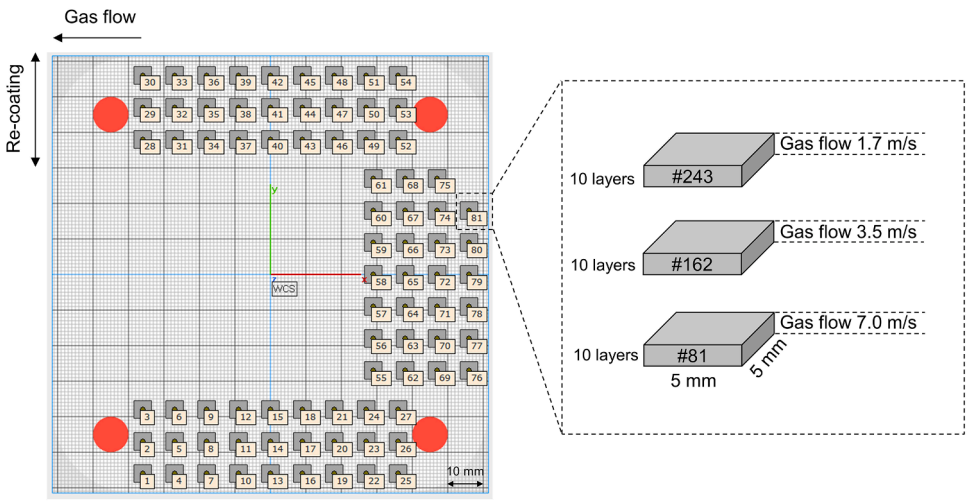

Fig. 1. Specimen layout on the building platform and specimen dimensions. The numbers (81, 162 and 243) illustrate how each specimen (numbered 1–81) is divided into three different samples of 5 × 5 × 0.3 mm, corresponding to the three different shielding gas flow levels along the build height. The red circles mark no-build zones (bolt holes for platform attachment), and black arrows mark re-coating and shielding gas flow directions.

i.e. the area to be scanned remains constant. Increasing scanning speed then decreases the samples collected by the MPM system per length of material scanned, respectively. The 99% confidence intervals calculated for the mean of the data were so small (0.001–0.006), that the error bars are not visible underneath the marker. This means very high confidence on where the calculated mean of the data really is. The number of samples for calculating the mean and confidence intervals was n = 172,055–527,939 depending on the specimen, see Table A1 in Appendix A.

Normalized enthalpy, as introduced in [22], is used to characterize the energy input to the process with the different combinations of laser parameters used. The calculation for normalized enthalpy is shown in Eq. (3), where p is laser power, v is laser scanning speed, a is beam diameter at work plane. The material constants used for the calculation in this study were absorptivity $\alpha = 0.4$, density $\rho = 8000$ g/cm^3, specific heat capacity $C = 800$ J/kgK, difference between initial and melting temperature $\Delta T = 1365$ K, latent heat of melting $L_m = 260$ kJ/kg and thermal diffusivity $D = 3.5 \times 10^{-6}$ m^2/s.

$$\overline{\Delta H} = \frac{\Delta H}{h_s} = \frac{\alpha P}{\rho(C\Delta T + L_m)\sqrt{\pi a^3 v D}} \tag{3}$$

3. Results and discussion

Fig. 2. shows linear correlation between laser power and all three photodiode signal outputs in the MPM system. The correlation between

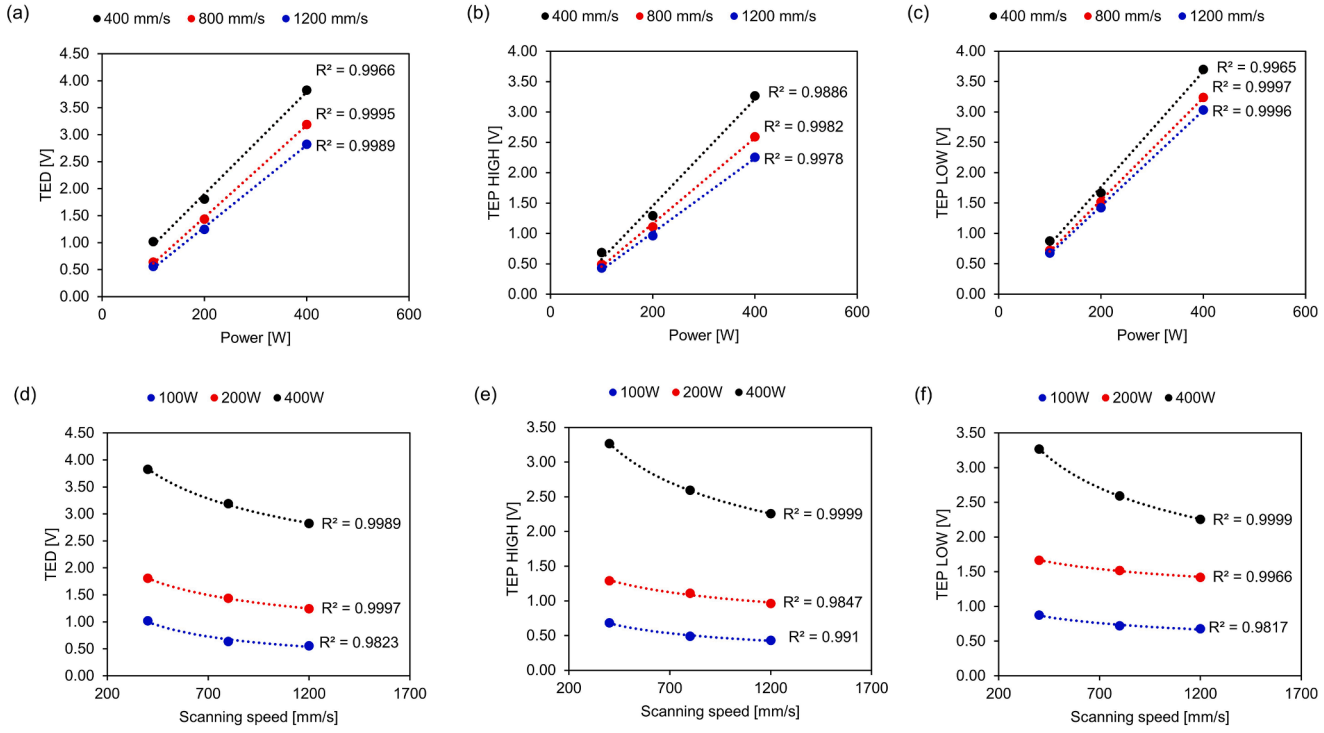

Fig. 2. Correlation of (a–c) laser power and (d–f) scanning speed with the MPM system photodiode responses. Dashed lines represent linear fit $ax+b$ for laser power, and ax^{-b} for scanning speed. The corresponding R^2 values displayed show excellent fit to the data.

laser scanning speed and the three photodiode signal outputs is non-linear. This is in very good agreement with experiments done on the resulting melt pool geometry by Metelkova et al. [23],where it was shown that the depth and width of the melt pool has linear correlation with laser power, while with the scanning speed the relation is non-linear. The relation to scanning speed is in the form of $y = ax^{-b}$, which could be also expressed as $y = \frac{a}{\sqrt[1/b]{x}}$. The trend becomes stronger with higher laser power, being almost non-existent with 100 W and with the highest laser power studied here (400 W), the constant b is 0.337. This agrees well with the physical relation established between melt pool size and scanning speed analytically using the concept of normalized enthalpy where the relation is $\frac{1}{\sqrt{v}}$. This also agrees very well with the observations made by Weaver et al. [24] and Naderi et al. [25], where it was shown that analytical models based on the concept of normalized enthalpy (having the relation $\frac{1}{\sqrt{v}}$) poorly correlate with melt pool dimensions during conduction melting, whereas with higher powers associated with keyhole mode melting the correlation significantly improves.

In Fig. 3 the focal point position is included as a variable, and the laser power, scanning speed and focal point position (via the beam diameter at work plane) are reduced to the singular parameter normalized enthalpy to allow for 2D-plots. All three photodiode signals in the MPM system behave in a similar manner. What is interesting to notice, is the separation of the responses when the focal point position is varied. Between the focus settings, the underlying trend remains as dictated by the response to laser power and scanning speed already shown in Fig. 2. This is highlighted in Fig. 3(c), where the individual laser power and scanning speed levels settings separate the data to different zones, rather than all collapsing to a singular trend. This is typical S-curve behavior, where there is a transition between levels, and within levels, a trend can be distinguished. And as now the scanning speed is modeled in the normalized enthalpy with the relation $\frac{1}{\sqrt{v}}$, the relation to the scanning speed seems close to linear. However, the response to the change of focal point position is not so straightforward, as a change in the focal point position (and hence beam diameter at work plane) significantly changes not only the temperature in the melt pool, but also the surface area of the melt pool. On one hand, defocusing the laser reduces melt pool temperature, but at the same time, it increases melt pool size. Photodiodes are sensitive to both the temperature and size of the emitting source. Hotter melt pool means increased (and higher energy) photon emission, and larger melt pool also increase photon emissions. Furthermore, the generation and removal of the vapor plume further has an impact on this, as explained later.

The effect of scanning angle on the TED signal is shown in Fig. 4. The response with TEP high and low was similar, and hence only one the signal from one of the photodiodes is used for plotting. With high energy densities (high normalized enthalpy, combined with focus position –4 or 0 mm), the scanning angle starts to have an impact on the photodiode signal, with a trend towards increased signal with reduced scanning angle. This is due to the presence of the vapor plume in high energy density conditions corresponding to keyhole formation, and the fact that the scanning orientation in relation to the cross-flow of shielding gas has an influence on how the vapor plume is cleared away from the optical path towards the photodiode [26] . The differences in the signal intensities between the extremes 0° and 90° is around ~20% in the most severe conditions. This effect is significantly smaller than with the laser power, scanning speed or focus position as shown previously. However, this variation is important to keep in mind when using the MPM system for quality assurance. Typically, in PBF-LB the laser vectors are rotated between layers, and hence the variation caused by the scanning direction should be taken into consideration as normal or baseline variation one can expect in the signal, and not to be confused with variations caused by un-wanted phenomena in the process.

The effect of shielding gas flow speed on the TED signal is shown in Fig. 5. The response with TEP high and low was similar, and hence only

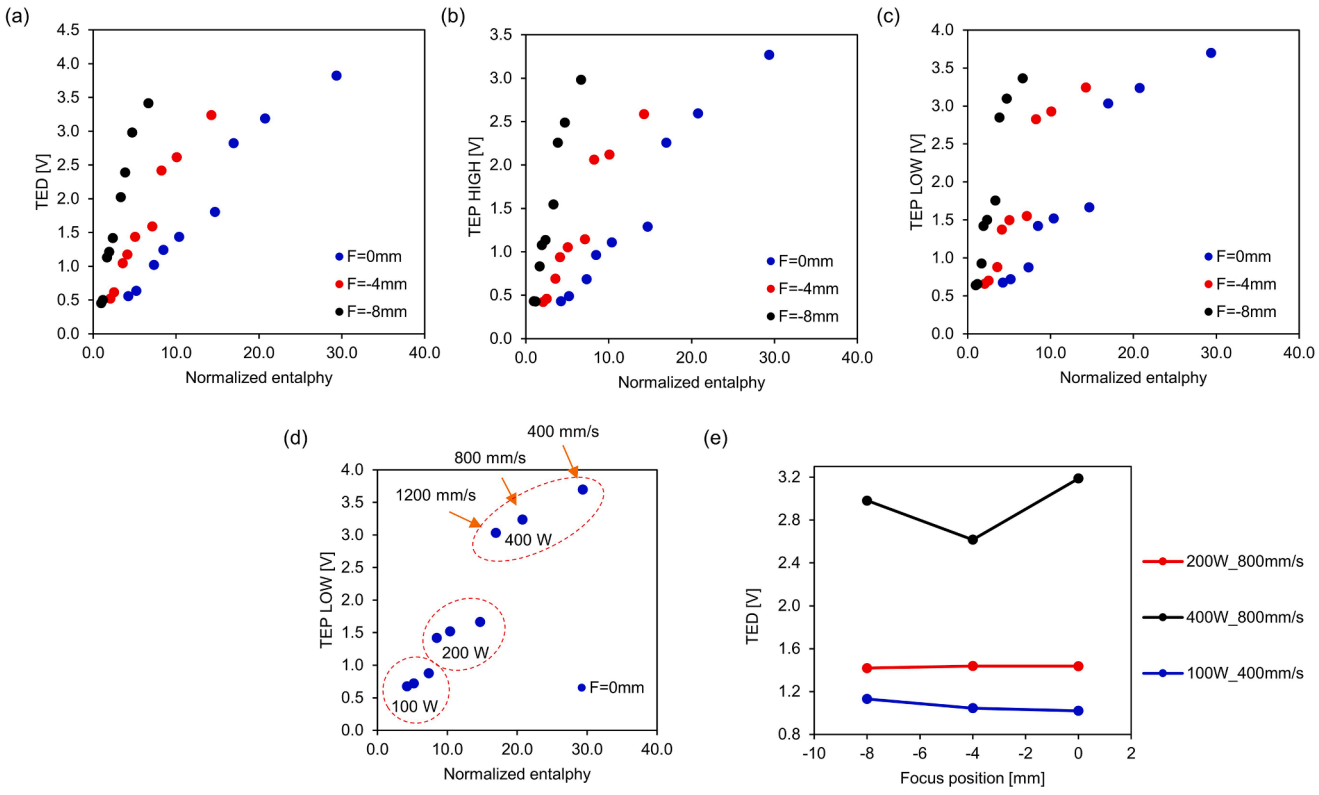

Fig. 3. MPM signal intensities (a–c) as a function of normalized enthalpy for the studied laser power, speed and focal point position combinations. In (d) the response of the signal to the laser power and scanning speed individually is highlighted, and in (e) the non-linear, and varying nature based on the used P/v combination of the effect of focal point position on the signal intensity is highlighted.

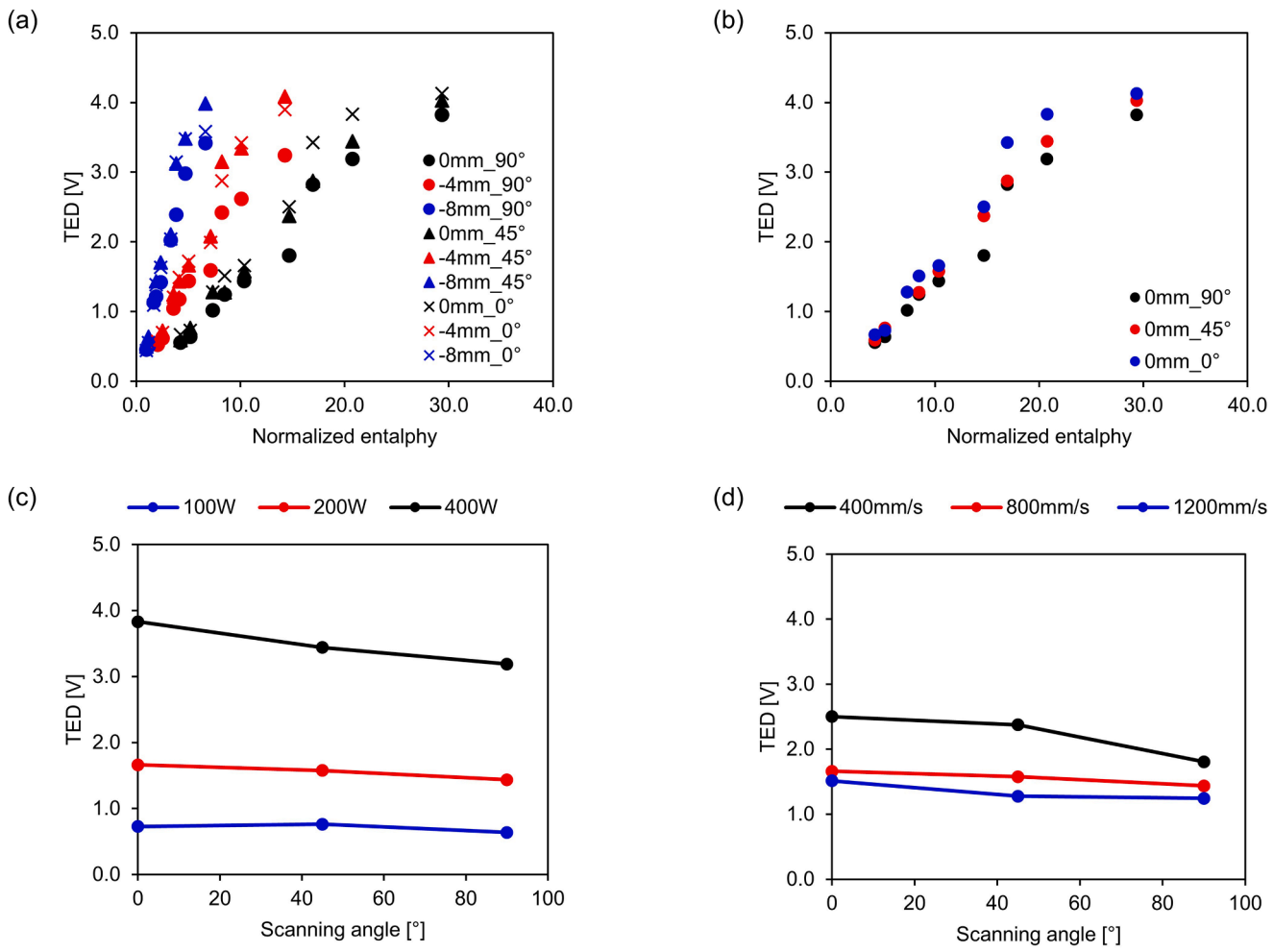

Fig. 4. Effect of scanning angle on the TED photodiode signal intensity (a–b) for various combinations of laser power, scanning speed and focal point position characterized by the normalized enthalpy, and (c–d) for laser power and scanning speed individually.

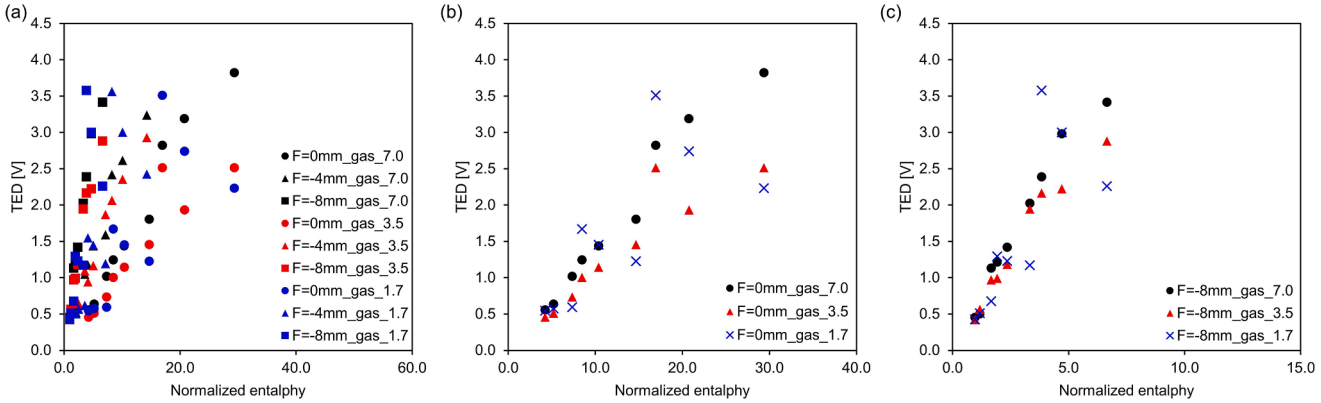

Fig. 5. Effect of shielding gas flow speed on the TED photodiode signal intensity at (a) all the studied normalized enthalpy conditions and (b–c) separate plots for 0 mm and –8 mm focus positions at different gas flow speeds to highlight the important differences. The colors indicate the shielding gas flow speed as black = 7.0 m/s, red = 3.5 m/s and blue = 1.7 m/s. Markers are utilized to enhance clarity.

the signal from one of the photodiodes is used for plotting. Fig. 5(a) first shows the TED signal intensity as a function of normalized enthalpy for all the studied laser parameter combinations. When compared to Fig. 3 (a) where the shielding gas flow speed was kept constant, it is evident that the shielding gas flow speed has an impact on the signal intensity as the data is much more scattered. To understand the underlying trends, couple of other plots are produced. First, in Fig. 5 (b and c) the TED signal response as a function of the gas flow speed (colors) is shown only for the nominal 0 mm focus position and the –8 mm defocus position. Here it can be clearly see the diverging behavior in the signal, when the gas flow speed is decreased. This becomes most evident when the gas flow is reduced to the 1.7 m/s setting (crosses in Fig. 5b and c), where the trend completely turns around. In the high 7.0 m/s gas flow conditions an increase in normalized enthalpy via adjustments in the *P/v*

always lead to an increased photodiode signal response, whereas in the slow 1.7 m/s gas flow conditions this trend turns, and an increase in the normalized enthalpy leads to *decrease* in the photodiode signal response. Furthermore, where this turn in the trend happens, depends on the normalized enthalpy and the focus position. When the energy density to the process is small (small normalized enthalpy), the photodiode signal response still increases along with increase in normalized enthalpy. Then, with high energy density to the process (high normalized enthalpy), this trends turns and a further increase in the normalized enthalpy just decreases the photodiode signal. The focal point position then has an impact on the threshold where the transition happens. In Fig. 5(c) where focal point position is –8 mm it is clearly seen that in the lowest normalized enthalpy conditions (corresponding to 100 W laser power) the photodiode signal is still increasing linearly for the gas flow condition 1.7 m/s. Then in Fig. 5(b) for the same 100 W conditions, but focal point position at 0 mm, the photodiode signal trend already starts to bend.

Fig. 6 further shows the impact of shielding gas flow speed on the TED photodiode signal at different laser powers and scanning speeds separately. Firstly, it is evident that in all shielding gas flow conditions, the positive linear correlation between the photodiode signal and laser power remains. However, depending on the associated scanning speed and laser power (i.e. normalized enthalpy) there is variation in the response to the shielding gas flow speed. This becomes most evident in Fig. 6 (d–f), where the photodiode signal is plotted as a function of scanning speed for three different power and shielding gas flow speed levels. In all conditions, the 1.7 m/s shielding gas flow condition has a completely different response. At low power of 100 W in Fig. 6(d), there is slightly decreasing trend in the 1.7 m/s condition, whereas for the 3.5 and 7.0 m/s conditions the decreasing trend is significant. Then, in Fig. 6 (e) with 200 W, the 3.5 and 7.0 m/s condition trends remain decreasing, but the 1.7 m/s condition produces a linearly increasing trend to the photodiode signal. This trend then remains for the 1.7 m/s condition in Fig. 6(f) with 400 W, however there it is seen that the response by the 3.5 m/s condition changes to that of a polynomial, first decreasing and then increasing again.

To explain this behavior in the signal as a function of the shielding gas flow in conjunction with the different laser power, speed and focal point position combinations, the schematic in Fig. 7 was produced. Essentially, this behavior relates to the fact that different process phenomena are present, and become more dominate, on certain parameter combinations. Specifically stated, the important factors are (i) whether the process is operated at conduction, transition or keyhole mode melting, (ii) whether there is vapor plume or not, and if yes, in what magnitude and inclined to what direction and (iii) how effectively the shielding gas flow removes this vapor plume from the optical path to the photodiode. Laser power, scanning speed and focal point position all have an impact on factors (i) and (ii), while the shielding gas flow speed mainly determines influence on the factor (iii). The shielding gas flow speed does, however, also have an impact on the melting mode and resulting melt pool geometry, as shown by Reijonen et al. [27], where loss of penetration, and increased melt pool width was associated with reduced gas flow speeds due to laser attenuation and scattering in the plume. Additionally, the scanning orientation in relation to the shielding gas flow (See Fig. 4) also has an impact on how the gas flow interacts with the plume [26], hence the impact on the photodiode signal. Furthermore, it is known that the vapor plume inclination angle is highly dependent on the scanning speed [28]. It is also known that an increase in laser power at constant gas flow speed will result in more severe vapor plume that is less effectively removed by the constant shielding gas flow speed [28]. Table 2 then provides a simplified summary of the relationships between the process parameters and the photodiode signal response.

Conclusions

Based on the results of this study, the following conclusions are drawn:

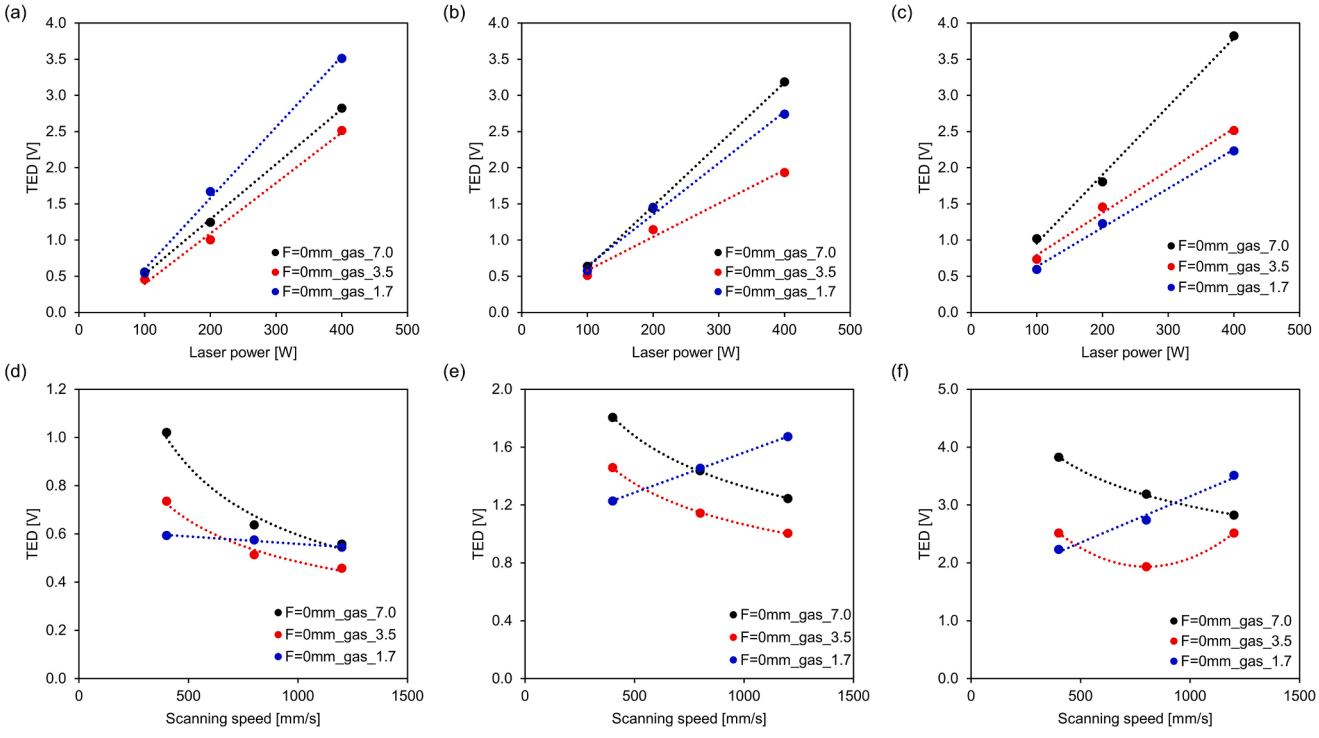

Fig. 6. Effect of shielding gas flow speed on the TED photodiode signal intensity at different laser powers, with scanning speeds constant at (a) 1200 mm/s, (b) 800 mm/s and (c) 400 mm/s; and with different scanning speeds while keeping the laser powers constant at (d) 100 W, (e) 200 W and (f) 400 W. The colors indicate the shielding gas flow speed as black = 7.0 m/s, red = 3.5 m/s and blue = 1.7 m/s.

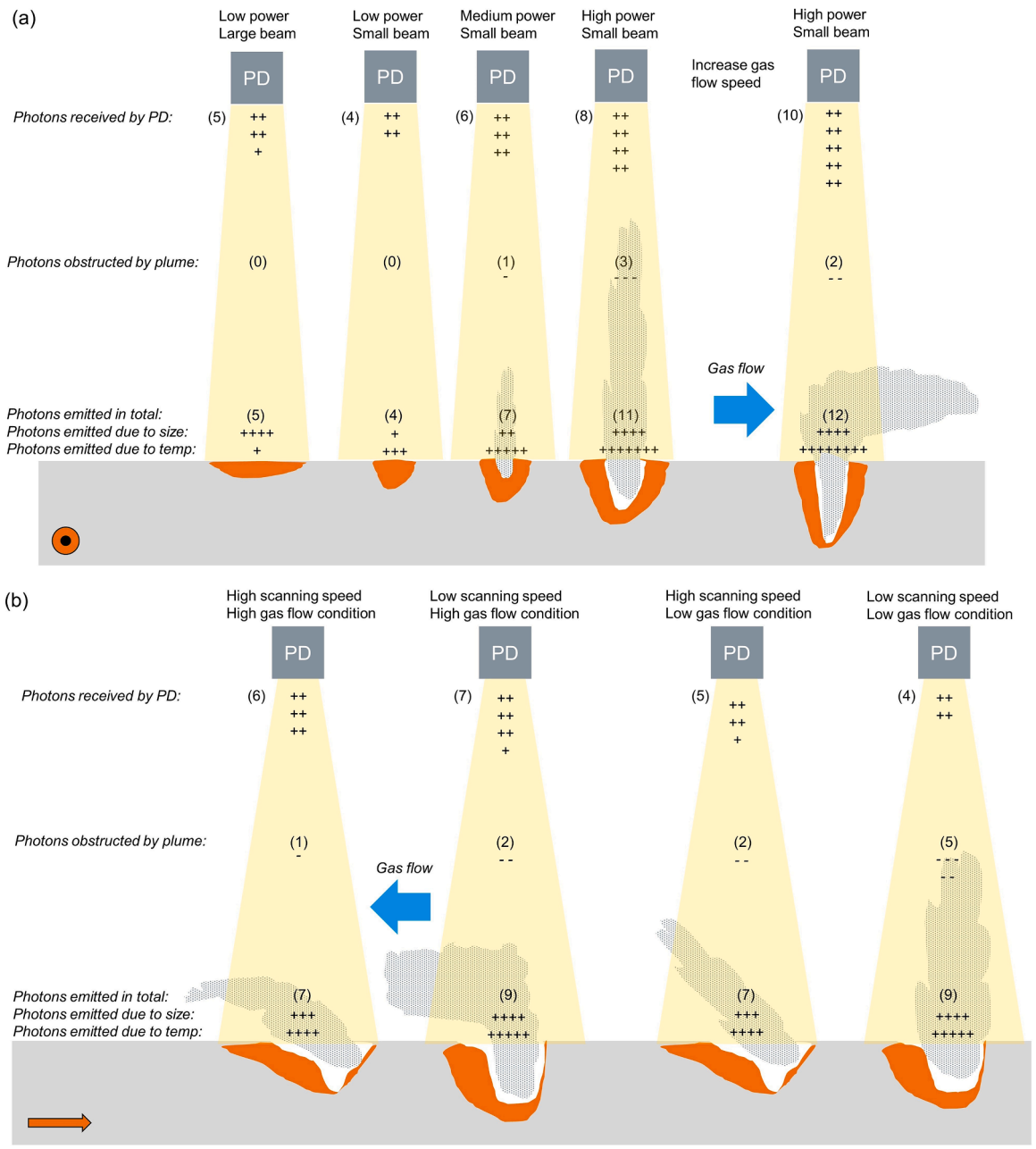

Fig. 7. Schematic illustration of the impact of different processing conditions to the emissions from the melt pool and to those received at the photodiode (PD). Photons are emitted (+ signs) from the melt pool due to the temperature and size, while photons are obstructed (- signs) by the vapor plume. The sum of this is the photons received at the photodiode, which would indicate the photodiode signal intensity. Possible photon losses due to attenuation in optical components and the spectral responsivity of the photodiode itself is not included in the schematic for simplicity. Arbitrary number of photons are drawn, with the intention of depicting either low, medium, high, or very high impact of the given phenomena on the photon count in each scenario. (a) shows scenarios with medium scanning speed, but varying laser power, beam size at work plane and gas flow conditions. (b) shows scenarios of increasing the scanning speed in low and high gas flow speed conditions. Red arrow indicates scanning direction and blue arrow shielding gas flow direction.

1. In the MPM system, all three photodiode signal intensities, whether wide or narrow band, have linear positive correlation with laser power.
2. With scanning speed, the correlation is non-linear, in the form of $y = ax^{-b}$, if gas flow speed is maintained sufficiently high to effectively remove the vapor plume.
3. The responses of the photodiode signals to laser power and scanning speed are in good agreement with the physical relation (as modeled via the normalized enthalpy) and the resulting impact they have on the melt pool. Therefore, the MPM signal intensity is a good indicator of the expected melt pool depth and width.
4. The impact of scanning angle of the laser vectors on the MPM signal was up to ~20% within the conditions tested in this study. This is important to take into consideration as normal variation in the signal intensity when building parts with PBF-LB and using photodiode-based MPM systems for quality assurance.
5. The impact of focal point position on the MPM signal is non-linear, and the response changes depending on the combination of laser power and speed used, as well as the shielding gas flow speed. This is due to the complex interplay between melt pool temperature, melt pool size and the magnitude of vaporization and hence the presence of vapor plume above the melt pool – all of which are dependent on

Table 2
Simplified summary of the impacts of the studied process parameters on the photodiode signal response.

Process parameter	Photodiode signal response	Physical phenomena behind the observation
Laser power	Positive linear $y = ax+b$	Increase in laser power increases melt pool temperature and melt pool size. Both increase the number of photons emitted from the melt pool and captured by the photodiode. Increasing laser power generates increased vaporization, however the magnitude of increased photon-obstruction by this vapor plume is less than the increase in total emissions from the melt pool.
Scanning speed	Non-linear $y = ax^{-b}$, if gas flow speed is high and constant. Trend hardly visible at low laser power	Increasing scanning speed decreases melt pool temperature and size. Both decrease the number of photons emitted from the melt pool and captured by the photodiode. In addition, decrease in scanning speed leads to decreased backward inclination of the ejected vapor plume. If shielding gas flow speed is insufficient to remove this plume from the path to the photodiode, the plume will obstruct some of the photon emissions. At low laser power corresponding to conduction mode melting there is no vapor plume and, in such conditions, the shielding gas flow speed has no impact to the photodiode signal.
Focal point position	Highly non-linear, response depends on laser power, scanning speed and gas flow speed	Deviating focal point position from beam-material interaction plane leads to increased effective beam diameter. This leads to increased melt pool size, but decreased temperature, hence there is a competing effect on the photodiode signal. Depending on the p/v used, also the absence or presence and magnitude of the vapor plume contributes to the signal. If vaporization is present, gas flow speed starts to have an impact. Therefore, depending on the combination of all the other parameters, an increase in focal point position may lead to either increase or decrease in the photodiode signal.
Gas flow speed	Highly non-linear, response depends on laser power, scanning speed and focal point position	With a combination of focal point position, laser power and scanning speed that result in conduction mode melting without the presence of a vapor plume, shielding gas flow speed has no impact on the photodiode signal. If the other parameters are selected such that vaporization is present, gas flow speed starts to have an impact. If scanning speed is altered, the change it produces on the plume inclination has an impact on the gas flow response. Therefore, depending on the combination of all the other parameters, a decrease in gas flow speed may lead to either increase, decrease or non-existent change in the photodiode signal.

the focal point position and will have an impact on the photodiode signal response.

6. The impact of shielding gas flow speed on the MPM signal is highly non-linear, and the response changes depending on the combination of laser power and speed used, as well as the focal point position. This is due to the complex interplay between melt pool temperature, melt pool size and the magnitude of vaporization and hence the presence of vapor plume above the melt pool – and how effectively the shielding gas flow can remove the vapor plume from the optical path to the photodiode.

Appendix A: error estimation

Table A1. Sample size, mean, standard deviation and 99% confidence interval of the mean for the MPM signal data for each specimen.

CRediT authorship contribution statement

Joni Reijonen: Writing – review & editing, Writing – original draft, Visualization, Methodology, Investigation, Formal analysis, Conceptualization.

Declaration of competing interest

The authors declare that they have no known competing financial interests or personal relationships that could have appeared to influence the work reported in this paper.

Data availability

Data will be made available on request.

Acknowledgements

The financial support of VTT Technical Research Centre of Finland is gratefully acknowledged. The author would like to thank Kimmo Ruusuvuori from VTT for the operation of the PBF-LB machine.

Supplementary materials

Supplementary material (Table A1) associated with this article can be found, in the online version, at doi:10.1016/j.addlet.2024.100244.

References

[1] Y.M. Wang, T. Voisin, J.C. McKeown, N.P. Ye, Z. Calta, Z. Zeng, Y. Zhang, W. Chen, T.T. Roehling, R.T. Ott, K. Santala, P.J. Depond, M.J. Matthews, A.V. Hamza, T. Zhu, Additively manufactured hierarchical stainless steels with high strength and ductility, Nat. Mater. 17 (2017) 63–71, https://doi.org/10.1038/nmat5021.
[2] L. Liu, Q. Ding, Y. Zhong, J. Zou, J. Wu, Y.L. Chiu, J. Li, Z. Zhang, Q. Yu, Z. Shen, Dislocation network in additive manufactured steel breaks strength–ductility trade-off, Mater. Today. 21 (2018) 354–361, https://doi.org/10.1016/j.mattod.2017.11.004.
[3] J. Berez, L. Sheridan, C. Saldaña, Extreme variation in fatigue: fatigue life prediction and dependence on build volume location in laser powder bed fusion of 17-4 stainless steel, Int. J. Fatig. 158 (2022) 1–14, https://doi.org/10.1016/j.ijfatigue.2022.106737.
[4] T.P. Moran, D.H. Warner, A. Soltani-Tehrani, N. Shamsaei, N. Phan, Spatial inhomogeneity of build defects across the build plate in laser powder bed fusion, Addit. Manuf. 47 (2021) 102333, https://doi.org/10.1016/j.addma.2021.102333.
[5] J. Reijonen, A. Revuelta, T. Riipinen, K. Ruusuvuori, P. Puukko, On the effect of shielding gas flow on porosity and melt pool geometry in laser powder bed fusion additive manufacturing, Addit. Manuf. 32 (2020) 101030, https://doi.org/10.1016/j.addma.2019.101030.
[6] M. Grasso, B.M. Colosimo, Process defects and in situ monitoring methods in metal powder bed fusion: a review, Meas. Sci. Technol. 28 (2017), https://doi.org/10.1088/1361-6501/aa5c4f.
[7] Z. Snow, L. Scime, A. Ziabari, B. Fisher, V. Paquit, Observation of spatter-induced stochastic lack-of-fusion in laser powder bed fusion using in situ process monitoring, Addit. Manuf. 61 (2023) 103298, https://doi.org/10.1016/j.addma.2022.103298.

[8] P. Mercelis, Control of Selective Laser Sintering and Selective Laser Melting Processes, Katholieke Universiteit Leuven, 2007.
[9] S. Clijsters, T. Craeghs, S. Buls, K. Kempen, J.P. Kruth, In situ quality control of the selective laser melting process using a high-speed, real-time melt pool monitoring system, Int. J. Adv. Manuf. Technol. 75 (2014) 1089–1101, https://doi.org/10.1007/s00170-014-6214-8.
[10] J. Reijonen, A. Revuelta, S. Metsä-Kortelainen, A. Salminen, Effect of laser focal point position on porosity and melt pool geometry in laser powder bed fusion additive manufacturing, Addit. Manuf. 85 (2024) 104180, https://doi.org/10.1016/J.ADDMA.2024.104180.
[11] K. Gutknecht, L. Haferkamp, M. Cloots, K. Wegener, Determining process stability of Laser Powder Bed Fusion using pyrometry, Procedia CIRP 95 (2020) 127–132, https://doi.org/10.1016/j.procir.2020.01.147.
[12] K. Gutknecht, M. Cloots, K. Wegener, Relevance of single channel signals for two-colour pyrometer process monitoring of laser powder bed fusion, Int. J. Mechatron. Manuf. Syst. 14 (2021) 111–127, https://doi.org/10.1504/IJMMS.2021.119152.
[13] C. Stutzman, A. Przyjemski, A.R. Nassar, Effects of gas flow speed on bead geometry and optical emissions during laser powder bed fusion additive manufacturing, Rapid Prototyp. J. 29 (2023) 1386–1394, https://doi.org/10.1108/RPJ-02-2022-0047.
[14] S. Lapointe, G. Guss, Z. Reese, M. Strantza, M.J. Matthews, C.L. Druzgalski, Photodiode-based machine learning for optimization of laser powder bed fusion parameters in complex geometries, Addit. Manuf. 53 (2022) 102687, https://doi.org/10.1016/j.addma.2022.102687.
[15] D. Alberts, D. Schwarze, G. Witt, In situ melt pool monitoring and the correlation to part density of Inconel® 718 for quality assurance in selective laser melting, in: Proc. 28th Solid Free. Fabr. Symp, 2017, pp. 1481–1494.
[16] J. Reijonen, A. Revuelta, H.P.N. Nagarajan, Towards data driven quality monitoring: alignment and correlation of photodiode-based co-axial melt pool monitoring signals to part quality in laser powder bed fusion, IOP Conf. Ser. Mater. Sci. Eng. 1296 (2023) 012009, https://doi.org/10.1088/1757-899X/1296/1/012009.
[17] S. Jayasinghe, P. Paoletti, C. Sutcliffe, J. Dardis, N. Jones, P.L. Green, Automatic quality assessments of laser powder bed fusion builds from photodiode sensor measurements, Prog. Addit. Manuf. 7 (2022) 143–160, https://doi.org/10.1007/s40964-021-00219-w.
[18] J. Li, L. Cao, H. Liu, Q. Zhou, X. Zhang, M. Li, Imbalanced data generation and fusion for in-situ monitoring of laser powder bed fusion, Mech. Syst. Signal Process. 199 (2023) 110508, https://doi.org/10.1016/j.ymssp.2023.110508.
[19] H. Zhou, C. Song, Y. Yang, V. Trofimov, In-situ monitoring of melt pool and signal modification in laser powder bed fusion, IEEE Sens. J. 23 (2023) 1, https://doi.org/10.1109/jsen.2023.3311092. –1.
[20] M. Bisht, N. Ray, F. Verbist, S. Coeck, Correlation of selective laser melting-melt pool events with the tensile properties of Ti-6Al-4V ELI processed by laser powder bed fusion, Addit. Manuf. 22 (2018) 302–306, https://doi.org/10.1016/j.addma.2018.05.004.
[21] B. Brandau, T. Mai, F. Brueckner, A.F.H. Kaplan, Angular dependence of coaxial and quasi-coaxial monitoring systems for process radiation analysis in laser materials processing, Opt. Laser. Eng. 155 (2022) 107050, https://doi.org/10.1016/j.optlaseng.2022.107050.
[22] D.B. Hann, J. Iammi, J. Folkes, A simple methodology for predicting laser-weld properties from material and laser parameters, J. Phys. D. Appl. Phys. 44 (2011), https://doi.org/10.1088/0022-3727/44/44/445401.
[23] J. Metelkova, Y. Kinds, K. Kempen, C. de Formanoir, A. Witvrouw, B. Van Hooreweder, On the influence of laser defocusing in Selective Laser Melting of 316L, Addit. Manuf. 23 (2018) 161–169, https://doi.org/10.1016/j.addma.2018.08.006.
[24] J.S. Weaver, J.C. Heigel, B.M. Lane, Laser spot size and scaling laws for laser beam additive manufacturing, J. Manuf. Process. 73 (2022) 26–39, https://doi.org/10.1016/j.jmapro.2021.10.053.
[25] M. Naderi, J. Weaver, D. Deisenroth, N. Iyyer, R. McCauley, On the Fidelity of the Scaling Laws for Melt Pool Depth Analysis During Laser Powder Bed Fusion, Integr. Mater. Manuf. Innov. 12 (2023) 11–26, https://doi.org/10.1007/s40192-022-00289-w.
[26] I. Bitharas, A. Burton, A.J. Ross, A.J. Moore, Visualisation and numerical analysis of laser powder bed fusion under cross-flow, Addit. Manuf. 37 (2021) 101690, https://doi.org/10.1016/j.addma.2020.101690.
[27] J. Reijonen, A. Revuelta, T. Riipinen, K. Ruusuvuori, P. Puukko, On the effect of shielding gas flow on porosity and melt pool geometry in laser powder bed fusion additive manufacturing, Addit. Manuf. 32 (2020) 101030, https://doi.org/10.1016/j.addma.2019.101030.
[28] P. Bidare, I. Bitharas, R.M. Ward, M.M. Attallah, A.J. Moore, Fluid and particle dynamics in laser powder bed fusion, Acta Mater. 142 (2018) 107–120, https://doi.org/10.1016/j.actamat.2017.09.051.